

# A Fast Surrogate Model for 3D-Earth Glacial Isostatic Adjustment using Tensorflow (v2.8.0) Artificial Neural Networks

Ryan Love<sup>1</sup>, Glenn A. Milne<sup>1</sup>, Parviz Ajournalou<sup>1</sup>, Soran Parang<sup>1</sup>, Lev Tarasov<sup>2</sup>, and Konstantin Latychev<sup>3</sup>

<sup>1</sup>Department of Earth Sciences, University of Ottawa, Ottawa, Ontario, Canada

<sup>2</sup>Department of Physics and Physical Oceanography, Memorial University of Newfoundland, St. John's, Newfoundland, Canada

<sup>3</sup>SEAKON, Toronto, Canada

**Correspondence:** Ryan Love (rlove@mun.ca)

**Abstract.** Models of glacial isostatic adjustment (GIA) play a central role in the interpretation of various geologic and geodetic data to understand and simulate past and future changes in ice sheets and sea level, and infer rheological properties of the deep Earth. During the past few decades, a major advance has been the development of models that include 3D Earth structure, as opposed to 1D, spherically symmetric (SS) structure. However, a major limitation in employing 3D GIA models is their high computational expense. As such, we have developed a method using artificial neural networks (ANNs) and the Tensorflow library to predict the influence of 3D Earth models with the goal of more affordably exploring the parameter space of these models: specifically the radial (1D) viscosity profile upon which the lateral variations are added.

Our goal is to test whether the use of an ANN to produce a fast surrogate model can accurately predict the difference in GIA model outputs (i.e., relative sea level (RSL) and uplift rates) for the 3D case relative to the SS case. If so, the surrogate model can be used with a computationally efficient SS (Earth) GIA model to generate output that replicates output from a 3D (Earth) GIA model. Evaluation of the surrogate model performance for deglacial RSL indicates that it is able to provide useful estimates of this field throughout the parameter space when trained on only  $\approx 15\%$  ( $\approx 50$ ) of the parameter vectors considered (330 in total).

We applied the surrogate model in a model:data comparison exercise using RSL data distributed along the North American coasts from the Canadian Arctic to the US Gulf coast. We find that the surrogate model is able to successfully reproduce the data:model misfit values such that the region of minimum misfit either generally overlaps the 3D GIA model results, or is within two increments of the radial viscosity model parameter space (defined here as lithosphere thickness, upper mantle viscosity, and lower mantle viscosity). The surrogate model can, therefore, be used to accurately explore this aspect of the 3D Earth model parameter space. In summary, this work demonstrates the utility of machine learning in 3D Earth GIA modelling and so future work to expand on this initial "proof of concept" analysis is warranted.

## 1 Introduction

Global models of glacial isostatic adjustment (GIA) have been in development since the 1970s and have several important applications (e.g., Spada, 2017; Whitehouse, 2018). Broadly speaking, through comparison of model output to a variety of

both geological and geodetic data sets, they can be used to improve our understanding of ice sheet and sea-level changes on  
25 decadal to 100 kyr timescales, and place constraints on rheological properties of the Earth's mantle. For example, geological  
reconstructions of relative sea level (RSL) provide key information on past changes in regional and global ice extent during  
the Quaternary (e.g., Milne, 2015). Calibrated GIA models are commonly used to predict and remove the contribution of this  
process to observations of contemporary RSL, land motion, and gravity changes. This is done in order to better isolate signals  
30 hydrology (e.g., Steffen et al., 2008; van der Wal et al., 2008; Wang et al., 2013).

To date, most GIA modelling studies have applied Earth models with a spherically symmetric geometry and so capture  
only variations in viscosity with depth. However, a variety of laboratory and geophysical investigations indicate strong lateral  
variability in Earth viscosity structure at all depths in the mantle (Karato, 2008). In the past few decades, a major improvement  
in the realism of GIA models has been the development of Earth models that can accommodate laterally variable viscosity  
35 structure (e.g., Latychev et al., 2005; Paulson et al., 2005; Wu, 2005; Klemann et al., 2007; Wang et al., 2008) resulting in what  
are referred to as '3D' Earth models. Since the development of these more realistic Earth models, a number of GIA studies  
have shown that the influence of lateral structure is important with respect to the applications outlined above (e.g., Paulson  
et al., 2007; Austermann et al., 2013; van der Wal et al., 2013, 2015; Kuchar et al., 2019). Therefore, it is important to continue  
to apply 3D models and improve constraints on Earth viscosity structure.

40 A primary limitation of 3D (Earth) GIA models (hereafter simplified to "3D GIA models") is their greater computational  
expense, which, in addition to the much larger parameter set associated with two additional spatial dimensions within the  
Earth model, makes exploring the parameter space a major challenge. As a result, determining the optimal parameter set and  
quantifying parameter uncertainty has not been done with any degree of rigour. The majority of studies that have applied 3D  
GIA models to date have focused on considering a relatively small number of 3D Earth viscosity models ( $\mathbf{O}(1-10)$ ) to consider  
45 the influence of the additional two dimensions on predicting surface observables (e.g., Whitehouse et al., 2006; van der Wal  
et al., 2015; Powell et al., 2021). In defining 3D mantle viscosity structure, most past studies have used global and/or regional  
seismic velocity models to infer lateral variability in viscosity, and a spherically symmetric (SS) model of viscosity variation  
on which to superimpose the lateral viscosity structure (e.g., Latychev et al., 2005; Wu et al., 2013). In most studies to date,  
only a handful,  $\mathbf{O}(1)$ , of these key model inputs have been explored. In comparison, studies focusing on the application of  
50 SS (i.e. 1D) Earth models often consider  $\mathbf{O}(100)$  viscosity models and/or order  $\mathbf{O}(1-10)$  ice loading histories to explore the  
model parameter space and map out the parametric uncertainty (e.g., Steffen and Kaufmann, 2005; Love et al., 2016; Caron  
et al., 2017). Recent studies using 3D Earth models have considered larger parameter sets (e.g., Bagge et al., 2021; Yousefi  
et al., 2021; Li et al., 2022; Pan et al., 2022), however, they remain limited sample sets of the complete Earth model parameter  
space. This incomplete exploration of the model parameter space is likely one of the reasons why the quality of data-model  
55 fits based on 3D Earth models has yet to improve substantially upon those obtained using 1D Earth models (e.g., Steffen et al.,  
2006; Spada et al., 2006; van der Wal et al., 2013; Li et al., 2018; Yousefi et al., 2021). One route to addressing this problem,  
in terms of identifying an optimal parameter set, is using adjoint methods (Crawford et al., 2018).

The work presented here is aimed at improving our ability to explore the parameter space of 3D GIA models via the use of a machine learning tool-chain to emulate the output from a 3D GIA model. Full emulation requires the generation of a predictive probability distribution for full model output given model inputs. In this study, an ANN is used to predict a single estimate of model output for specified input, and so the term "surrogate model" is more appropriate than "emulator". However, we often use the term emulator instead of surrogate model to improve clarity and readability. This approach has been employed successfully in other disciplines where model computational expense has been a limiting factor in exploring the parameter space (Tarasov et al., 2012; Sellevold and Vizcaino, 2021; Williams et al., 2023). A recent study (Lin et al., 2023) applied a graph-based spherical convolutional neural network algorithm to the GIA problem. Their focus was on emulating RSL on a single 1D Earth model for a wide range of ice history models, and so very different to the aims of this study. Given the high computational efficiency of the 1D GIA model, a relatively large training set of 1200 simulations was used in their analysis. In general, good results were obtained indicating the potential utility of ANN methods in GIA applications. A primary challenge for the 3D case considered here is the much reduced computational efficiency, limiting the number of simulations that can be performed to generate a training set.

We view this study as developing a "proof of concept" that future studies can build upon. In this regard, we have chosen to focus this work on optimising one of the key inputs to a 3D GIA model. Specifically, for a given model of lateral structure (lithosphere and seismic model) and ice loading, we seek to determine if it is possible to successfully emulate model output for  $\approx 300$  different SS reference viscosity models based on a relatively small training set ( $\mathbf{O}(10 - 100)$ ) simulations). Our results indicate that sufficiently precise emulation can be achieved with a training set of  $\approx 40 - 60$  simulations, resulting in a computational (wall) time saving of  $\approx 85\%$ . Given this success, we considered an application of the emulator based on a typical GIA dataset - geological (proxy) reconstructions of RSL - to seek an optimal SS reference viscosity model for our chosen models of lateral lithosphere thickness and sub-lithosphere viscosity variations. Our inference of the optimal SS viscosity model parameters using the emulator is close to that inferred using output from the numerical 3D GIA model, thus indicating the potential of the ANNs to more efficiently search the 3D Earth model parameter space.

## 2 Experimental Design & Methods

Here we describe the individual components of the numerical models and overall experimental design of this investigation. We introduce, in Sect. 2.1, the individual models used, and then the method by which model output is processed to produce training data (Sect. 2.2). We then provide some details on the implementation and training of the artificial neural networks (ANNs, Sect. 2.3). Finally, we outline the data used in the proxy-data:model comparison (Sect. 2.4).

### 2.1 GIA/RSL Models

We use two separate GIA models to compute RSL and radial displacement. Both solve the sea level equation (Farrell and Clark, 1976; Mitrovica and Milne, 2003; Kendall et al., 2005) and model the solid Earth response to the loading and unloading of the Earth's surface through time. They each have equivalent feature-sets with respect to the inclusion of compressibility (Wu and

90 Peltier, 1982), migrating shorelines (Milne and Mitrovica, 1998; Mitrovica and Milne, 2003), and rotational feedback (Milne  
and Mitrovica, 1998; Mitrovica et al., 2005). However, the computational methods are different: the model that can accomodate  
3D Earth structure uses a numerical Finite Volume approach (Latychev et al., 2005), whereas the simpler and computationally  
less expensive 1D GIA model relies on the computation of visco-elastic Love numbers (Peltier, 1974) for a specified radial  
structure (density, elastic moduli, viscosity). Once the Love numbers have been computed (e.g., via a normal mode analysis,  
95 Peltier, 1976; Mitrovica and Peltier, 1992), calculation of various GIA observables, such as RSL, is computationally efficient  
(Mitrovica and Peltier, 1991). Hereafter this model will be referred to as the normal mode SS model (abbreviated to NMSS  
model). A model run of glacial cycle duration typically requires less than 0.5 core-hours<sup>1</sup> on contemporary computer hardware  
(surface resolution being a key factor in determining the computational time). As a result of this computational efficiency,  
large scale sampling the GIA model parameter space is feasible with recent studies presenting results for many thousands of  
100 simulations exploring the parameter space of Earth model and ice-sheet reconstructions (e.g. Steffen and Kaufmann, 2005;  
Love et al., 2016; Caron et al., 2017). The more complex and computationally expensive model that we use here - the Seakon  
model of Latychev et al. (2005) - does not have the limiting assumption of a spherically symmetric Earth structure. However,  
this model requires  $\approx 1.75$  core-years for a typical glacial cycle experiment, which precludes its use for generating large  
ensembles of model output. Contemporary investigations with the Seakon model are limited to ensembles of several dozen  
105 (e.g., Pan et al., 2022) and more typically fewer than a dozen simulations.

To define a 3D viscosity structure in the Seakon model, lateral viscosity variations are applied on top of a chosen spherically  
symmetric (radial) viscosity model. Here we employ a commonly-used 3-layer parameterization of this spherically symmetric  
viscosity structure, as in the NMSS model, composed of a high-viscosity (i.e., elastic) lithosphere above two regions with  
uniform viscosity. These two regions are the upper mantle (base of lithosphere to  $\approx 670$  km depth) and lower mantle ( $\approx 670$  km  
110 to  $\approx 2900$  km depth). Sub-lithosphere lateral variations are applied via a set of relationships between shear-wave velocity  
anomalies and various depth-dependent parameters (Latychev et al., 2005, see Equations 27 through 29). Lateral lithosphere  
variations can be introduced using constraints that are independent of the adopted global seismic model (see next section) and  
are represented as a viscoelastic layer of varying thickness with a very high ( $1 \times 10^{37}$  Pa · s) viscosity such that the response is  
essentially that of an elastic material on GIA timescales.

115 In order to increase the number of parameter vectors (i.e., model runs) which can be examined with the available com-  
putational resources, we use a reduced resolution configuration of the Seakon model. The reduced resolution configuration  
has a horizontal surface resolution of  $\approx 33$  km and uses  $\approx 6$  million nodes vs.  $\approx 15$  km and  $\approx 17$  million nodes for the default  
configuration. This change results in a reduction of core-time to  $\approx \frac{1}{3}$  of the default configuration. Comparing model output  
of RSL using these two grids at various times indicates that differences are generally largest at the last glacial maximum  
120 ( $\approx 20,000$  years ago; Fig. S1), reaching an amplitude of  $\approx 5$  m, and diminish for later times. Given the limited spatial resolu-  
tion of inputs to Seakon (e.g., ice and seismic models), we consider the lower resolution grid to be sufficiently accurate for the

---

<sup>1</sup>core-hours and core-years are equivalent to 1 hour (or year) of a CPU core at full utilization, here we generally use either Intel Xeon E5-2683 v4 Broadwell  
processors clocked at 2.1 GHz or AMD EPYC 7401P processors clocked at 2.0 GHz.

purpose of this analysis. As a result, with Seakon we were able to explore all 330 combinations of LT/UMV/LMV for which we have calculated the required Love numbers for the NMSS model, representing  $\approx 150$  core-years of computational resources.

125 Despite the broad overlap in function of the Seakon and NMSS models, they have distinct roles in this investigation. We seek to train an ANN to simulate the difference in model output between Earth models with 3D and SS structure. The Seakon numerical model is used (in 3D and SS configurations) to generate this model output. We used the Seakon code in SS configuration rather than the NMSS code to avoid introducing any error in the calculated 3D-1D signal due to differences between output of the Seakon and NMSS codes (for the same 1D configuration). Once the ANN is successfully trained, generating model output for a 3D Earth model is achieved by simply adding the ANN-derived 3D-1D signal to output from an efficient 130 NMSS model with the relevant SS structure. Thus, the Seakon model is used to generate the training and validation data for the ANN. Output from the NMSS model was used only to convert the differential (3D-1D) signal to the full 3D signal (for both explicitly modelled (Seakon) and emulated (ANN) output).

## 2.2 Generation of Model Training Inputs using the Seakon Numerical Model

The Seakon model is used in both SS and 3D Earth model configurations to produce the input datasets used to train the ANNs. 135 The SS configuration (i.e., parameters varying only with depth) is used to compute the differential (3D minus 1D) signal. The primary configurations of the Seakon model used in this investigation are as follows:

1. Spherically symmetric (i.e. varying only with depth and defined by 3 variables: LT, UMV, and LMV, as defined previously).
- 140 2. Spherically symmetric perturbed using S-wave velocities from the S40RTS model [S40RTS] (Ritsema et al., 2010, plots of relative viscosity variations are shown in Fig. 1).
3. Spherically symmetric perturbed using S-wave velocities from the S40RTS model with the addition of laterally variable lithosphere thickness from the LR18 lithosphere model [S40RTS+LR18] (Ritsema et al., 2010; Afonso et al., 2019, plot of lithosphere model LR18 is shown in Fig. 1).
- 145 4. Spherically symmetric perturbed using S-wave velocities from the Savani model with the addition of laterally variable lithosphere thickness from the LR18 lithosphere model [Savani+LR18] (Auer et al., 2014; Afonso et al., 2019, plot of relative viscosity variations is shown in Fig. S2).

The (full 3D) S40RTS+LR18 configuration is used to explore the application of ANNs considered here and for the proxy-data:model comparison. The Savani+LR18 configuration is used to examine the impact of an alternative laterally variable viscosity model on the ANN training and misfit results. The semi-3D S40RTS configuration is used to examine the impact 150 of the inclusion of a laterally variable lithosphere model on the ANN results, via a comparison to the S40RTS+LR18 results. The SS configuration of Seakon is used throughout the investigation to determine the differential 3D-SS output on which the ANNs are trained and tested (as detailed below). Within each of the SS configurations we explore the parameter space of elastic lithosphere thickness (LT) as well as upper and lower mantle viscosities (UMV, LMV). The ranges of LT (71 – 120 km),

UMV ( $0.05 - 5 \times 10^{21}$  Pa · s), and LMV ( $1 - 90 \times 10^{21}$  Pa · s) values used in this study are in line with previous studies which  
155 constrain these values (e.g., Lambeck et al., 2014; Roy and Peltier, 2017). The parameter space of LT, UMV, and LMV values is  
sampled using a Latin hypercube scheme with the goal of maximizing parameter space coverage within computational resource  
limitations. As a result, from the combined total of 330 realizations for each Seakon configuration (e.g., S40RTS+LR18), up to  
63 parameter vectors were drawn to train the ANNs while the remainder were used only for comparison against the emulator  
output. The configurations from which training and validation data is drawn use the same ice loading history: ICE6G (Peltier  
160 et al., 2015; Roy and Peltier, 2017). In total, considering both SS and 3D cases, the Seakon numerical model was run 1,320  
times for this analysis (i.e., 330 runs for each of the four configurations defined above).

Preliminary results (not shown here) indicated that emulation based on the rate of change (ROC), with respect to time, of  
the 3D-SS difference resulted in smaller prediction misfits compared to emulating RSL or radial displacement (RAD) directly.  
Therefore, these are the model datasets considered in the remainder of this analysis. Given that RSL is defined to be zero at  
165 present day, we can readily recover the full timeseries of the field by integrating the ROC from the present.

For each 3D-SS parameter vector we then sample the ROC of RSL (or RAD) at one degree regular spacing in both latitude  
and longitude for each model time-step (from 36 ka to present, 59 time-steps in total). From each parameter vector (PV) we  
extract the ROC of RAD & RSL from files constructed for model performance evaluation (or training without any filtering).  
The values of ROC of RAD & RSL are then concatenated across all PVs, and then evaluated using the numpy histogram  
170 function to generate probability density functions of ROC of RSL & RAD. This global (with respect to space, time, and Earth  
model parameters) distribution is then used to re-sample the GIA model output data points of each parameter vector for more  
effective and efficient training of the ANNs. The re-sampling/filtering is implemented such that the most common values, i.e.,  
those 3D-1D ROC values closest to zero, largely located in far-field regions, have their occurrence reduced by several orders of  
magnitude in the training data. This filtering reduces the input training dataset from  $\approx 4,600,000$  to  $\approx 500,000$  data-points per  
175 ensemble member (i.e., LT-UMV-LMV parameter vector for a given 3D-1D configuration). The net result of this processing  
is a reduction of network training time, computer memory requirements, and increased quality of fits in regions with larger  
(3D-1D) ROC RSL or ROC RAD anomalies (i.e., near- and intermediate-field locations). Each parameter vector results in  
unique input training (i.e., filtered) and comparison (i.e., unfiltered) dataset files. These files are then combined as required into  
a single datafile for either training or comparison purposes.

### 180 2.3 Training of the ANNs

The training and implementation of the ANNs is accomplished via the Tensorflow framework (v2.8.0, Abadi et al., 2015).  
The choice of framework/library was motivated by the available support at the high performance computing center where the  
network training was conducted. We anticipate that comparable results can be achieved with other frameworks. Using the  
datasets described in Sect. 2.2, we train separate ANNs for each of the combinations of laterally variable earth structure (i.e.,  
185 S40RTS, S40RTS+LR18, Savani+LR18) and ice sheet history (i.e., ICE6G). As a result, each combination of laterally variable  
earth structure and ice sheet history produces a separate set of ANN weights to be used with the emulator. The inputs to the  
ANNs can be grouped into 4 aspects: radial viscosity model, location, ice loading, and SS input data. More specifically:(1) LT,

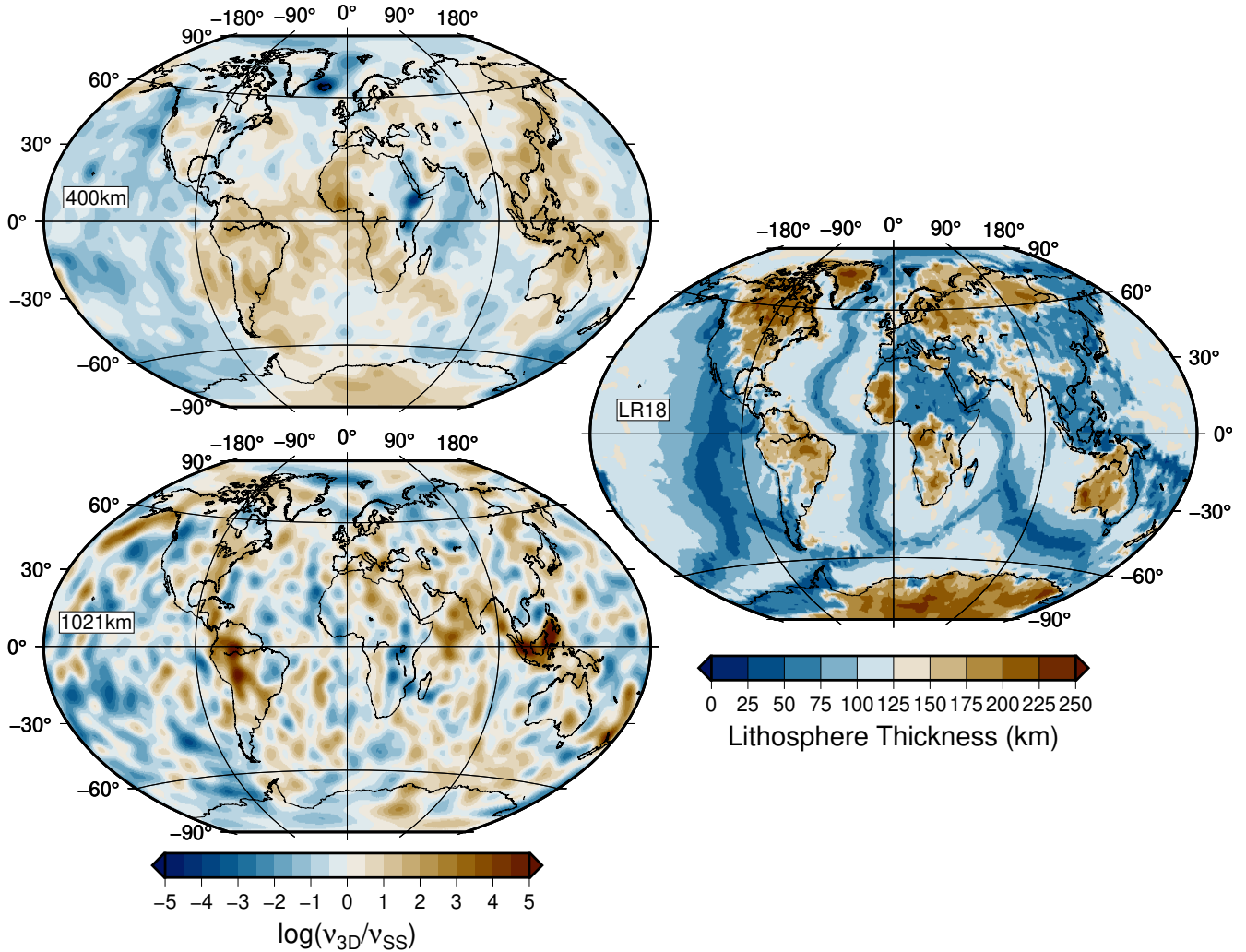


**Figure 1.** Left-hand panels show spatial viscosity variations as  $\log(\nu_{3D}/\nu_{SS})$  for two depths in the mantle, 400 km and 1021 km. A value of zero indicates that the viscosity value at that location is equivalent to the background spherically symmetric Earth model. Right-hand panel shows the lithosphere thickness distribution of the LR18 model. Note that these thickness values are scaled such that the global average thickness is equivalent to the value specified in the SS configurations. The scaling depends on the target global value for the ‘reference’ 1D viscosity profile. For most cases, the scaling is less than 1 and so the values shown are significantly reduced (by  $\approx 10 - 40\%$ ).

(2) UMV, (3) LMV, (4) longitude, (5) latitude, (6) ice thickness values and timing for the current and four previous time steps, (7) ROC of RSL or RAD prediction from the SS configuration of the Seakon model.

190 The prediction of the ANNs is the 3D-1D anomaly for the ROC of either RSL or RAD at the location and time which corresponds with the input to the ANN. Prior to training, the input dataset is split into the online training and validation sets, with 75% of the input data used in training and the remaining 25% used for validation. As discussed, the training data is already filtered at this stage to emphasize regions with greater amplitude signals. Within the context of model training the ‘validation set’ is used only for monitoring the ANN training for evidence of over-fitting and contains data from all PVs included in the  
195 input dataset. ANN training and model construction (i.e., specification of size and number of hidden layers) is done via the Keras Application Programming Interface. Training of an individual ANN usually requires no more than a dozen hours of wall time using a single NVIDIA P100 Pascal Graphics Processing Unit (GPU). The training of a given ANN is iterated until an early stopping condition, based upon the mean square error (MSE) of the ANN prediction against the training dataset, is activated. This early stopping condition for RSL is set such that, if there is no improvement of the MSE by at least  $0.01 \text{ (mm/yr)}^2$  within  
200 50 training epochs, the training stops and the set of weights which results in the lowest MSE is chosen. This approach is used to prevent, or at least minimize, over-fitting of the trained ANNs (Chollet, 2021). We note there was no evidence of over-fitting in the training diagnostics. The choice of using the previous 4-time steps was motivated by preliminary testing and evaluating trade-offs with respect to hardware limitations and quality of predictions. Generally, providing more previous timesteps to the networks resulted in reduced misfits, but there were rapidly diminishing returns and technical issues (largely due to memory  
205 and storage constraints on the hardware used for training) with adding significantly more past time-step data. Four previous timesteps were found to be a useful balance between model expense and useful predictions.

With the Keras Application Programming Interface we construct multi-layer perceptron feed-forward ANNs. The structure of the ANN is composed of an input layer, 8 fully connected hidden layers of width 512, followed by 8 fully connected hidden layers of width 256, followed by the output layer. Between the fully connected hidden layers are normalization layers which  
210 shift and scale their inputs such that the resulting distribution has a mean of 0 and a standard deviation of 1. The addition of the normalization layers helped with convergence of the network as network depth (i.e., model layer count) increased. A variety of ANN structures were evaluated; for example: layer counts from 2 to 20 layers and widths from 8-1024, in steps of  $2^n$ , were varied using an initial test dataset. Some results from these initial explorations are summarized in Fig. S3 which shows ROC RSL MSE for ANNs with network widths of 64 to 1024 nodes, and fully connected hidden layers (with normalization layers)  
215 between 2 and 10. Optimal results were generally found for network widths of 512 and 1024, and depths of 8 or 10. The configuration outlined above provides a good balance between performance and training expense. The Python scripts used for training and implementing the ANNs and for producing various GIA predictions are available as supplemental materials.

## 2.4 Model:Data Comparison - Source Data and Analysis Methods

For the RSL proxy-data:model comparison we use the RSL databases of Engelhart and Horton (2012), Love et al. (2016),  
220 and Vacchi et al. (2018), which spans the eastern North American coastline from the Canadian Arctic to the US Gulf Coast.



Combined, these databases contain > 2500 sea level index and limiting points. The locations of these data points are shown in Fig. S4.

In order to quantify the data-model RSL misfits we use the same metric as in Baril et al. (2023) for sea level index points (SLIPs) and limiting data, reproduced here for reference.

$$225 \quad \delta_{SLIP} = \frac{1}{N} \sqrt{\sum_{n=1}^N \left( \frac{RSL_{data,n} - RSL_{model,n}}{\Delta_{RSL,n}} \right)^2 + \left( \frac{t_{data,n} - t_{model,n}}{\Delta_{t,n}} \right)^2} \quad (1)$$

$$\delta_{limit} = \frac{1}{N} \sqrt{\sum_{n=1}^N \left( \frac{RSL_{data,n} - RSL_{model,n}}{\Delta_{RSL,n}} \right)^2} \quad (2)$$

In equation 1, the  $RSL_{model,n}$  and  $t_{model,n}$  values are the model RSL and time-value from the point of closest approach of the model curve to the value of the SLIP. However, for limiting data, the misfit (equation 2) is calculated using the same time value  
 230 as the data point itself. In the case of limiting data, if the RSL curve for a given model falls above/below a marine/terrestrial data point within the range of dating uncertainty, then the misfit for that data point is set to zero (Baril et al., 2023). When examining the total  $\delta$  for a given RSL database, the following values are provided:  $\delta_{SLIP}$ ,  $\delta_{ML}$ ,  $\delta_{TL}$ , and  $\delta_{Total}$ . Where  $\delta_{SLIP}$  is the value from equation 1 for a given SLIP database,  $\delta_{ML}$  and  $\delta_{TL}$  are the values from equation 2 for marine and terrestrial limiting data respectively, and  $\delta_{Total} = \delta_{SLIP} + (\delta_{ML} + \delta_{TL})/2$ . Contributions from limiting data are normalised by two since  
 235 these data only provide one-sided constraints on RSL.

### 3 Results and Discussion

#### 3.1 Network Training and Performance

In this section we determine how many parameter vectors (LT/UMV/LMV) are required in the training set to obtain useful predictions from the emulator (we use ‘emulator’ here to refer to the combination of trained ANNs with output from the NMSS  
 240 model). In order to estimate this number we construct several Seakon (3D-1D) ensembles consisting of increasing quantities of parameter vectors in the training dataset. These ensembles were determined using the S40RTS model to construct lateral viscosity variations in the mantle with lithosphere variations derived from the LR18 model. Each trained ANN incorporated the same core set of 9 extreme ensemble members (i.e., members that include LT/UMV/LMV parameter values at the beginning or end of the ranges defined in Sect. 2.2). Additional supplemental parameter vectors were added to this baseline set, with 9, 18,  
 245 36, and 54 members each. The lowest number of 9 supplemental parameter vectors was used to determine if we could accurately predict the 3D-SS difference as a function of LT/UMV/LMV with only the core parameter vector set and a single intermediate parameter vector between each of these end-member cases (18 parameter vectors in total; 9 core plus 9 supplemental). From there we doubled the supplemental set to 18 and subsequently 36. Finally, rather than doubling the number of supplemental parameter vectors a third time, we defined an upper limit of 54 based on the rationale that requiring a larger training set would

250 not be sufficiently resource-effective. Combining the core and supplemental sets resulted in 4 trained networks with  $N = 18$ , 27, 45, and 63 members, respectively. To quantify the generalization of the ANNs (i.e., their accuracy with respect to parameter vectors not in the training ensemble) as a function of training ensemble size, the mean square error (MSE) for each parameter vector in the LT/UMV/LMV space is calculated. The MSE for a given parameter vector is averaged over all locations and time-steps (i.e., the full dataset described in Sect. 2.2).

255 Plots of the MSE for the S40RTS+LR18 configuration through the LT/UMV/LMV parameter space for the ROC RSL are shown in Fig. 2 for the different training sub-ensembles (results for  $N = 18$  are not shown). It is notable that the reduction in the MSE in going from  $N = 27$  to  $N = 45$  is more marked compared to the change from  $N = 45$  to  $N = 63$ . This indicates that  $N = 45$  is close to an optimal value in terms of performance (lowering the MSE) versus the size of training set. In general, throughout the parameter space, the MSE decreases as the number of members in the training set increases (this is particularly  
260 evident when considering the median and lowest MSE values). Furthermore, Fig. 2 shows that the thickness of the elastic lithosphere is generally a weak predictor of the 3D-SS ROC RSL. In general, regions in the parameter space that have at least one member in the training ensemble, independent of the LT value, have lower MSE values compared to those with none. This finding is also supported by the input layer weights, where LT is consistently the lowest weight input (and thus has the lowest impact on predictions) when training ANNs. Figure 2 also shows that prediction accuracy for a given parameter vector  
265 is generally larger when it is adjacent to another which is part of the training ensemble. As such, the distribution of training parameters is an important consideration when training the ANNs. These results indicate that the ANN has useful levels of predicative ability when considering LT/UMV/LMV values outside the training dataset.

Comparing the results in Fig. 2 to those for the other fully 3D configuration, Savani+LR18 (Fig. S5), indicates that these findings are valid across different velocity models. The MSE decreases as  $N$  increases, though the MSE does not appear to  
270 decrease with  $N$  as quickly as for the S40RTS+LR18 configuration. The overall lateral viscosity structure of the Savani+LR18 configuration is not significantly different from that of the S40RTS+LR18 configuration (select layers shown in Figs. S2 and 1). As such, it is not immediately clear why there is a difference in MSE for the same values of  $N$  for different 3D Earth models. However, the general success of applying this method to two fully 3D Earth models indicates that this approach should be generally applicable regardless of the adopted velocity model. However, this preliminary conclusion should be investigated  
275 further in future work.

Despite the MSE of the full spatio-temporal datasets being a useful metric for comparing between different ANN architectures and training ensembles, it is of limited utility in describing the effectiveness of a given ANN in reproducing the geophysical output of interest. Therefore, plots showing the difference between emulated output versus modelled output (for S40RTS+LR18) are provided for the RSL field at 10 ka (Figs. 3 and S6, for eastern North America and global domains respectively) and the uplift rate at present day (Figs. 4 and S7, for eastern North America and global domains respectively). They  
280 show RSL and ROC RAD predictions for the parameter vector which has the median MSE from the validation (i.e., not used as part of the ANN training) sub-ensemble for the  $N = 45$  case.

Comparing the scale of emulator:model anomaly to the RSL field itself (Fig. 3) we see that the misfit is  $\mathbf{O}(1\text{ m})$  where generally the RSL field itself is generally  $\mathbf{O}(10 - 100\text{ m})$ . The intermediate-field region (e.g., proximal and south of the zero-

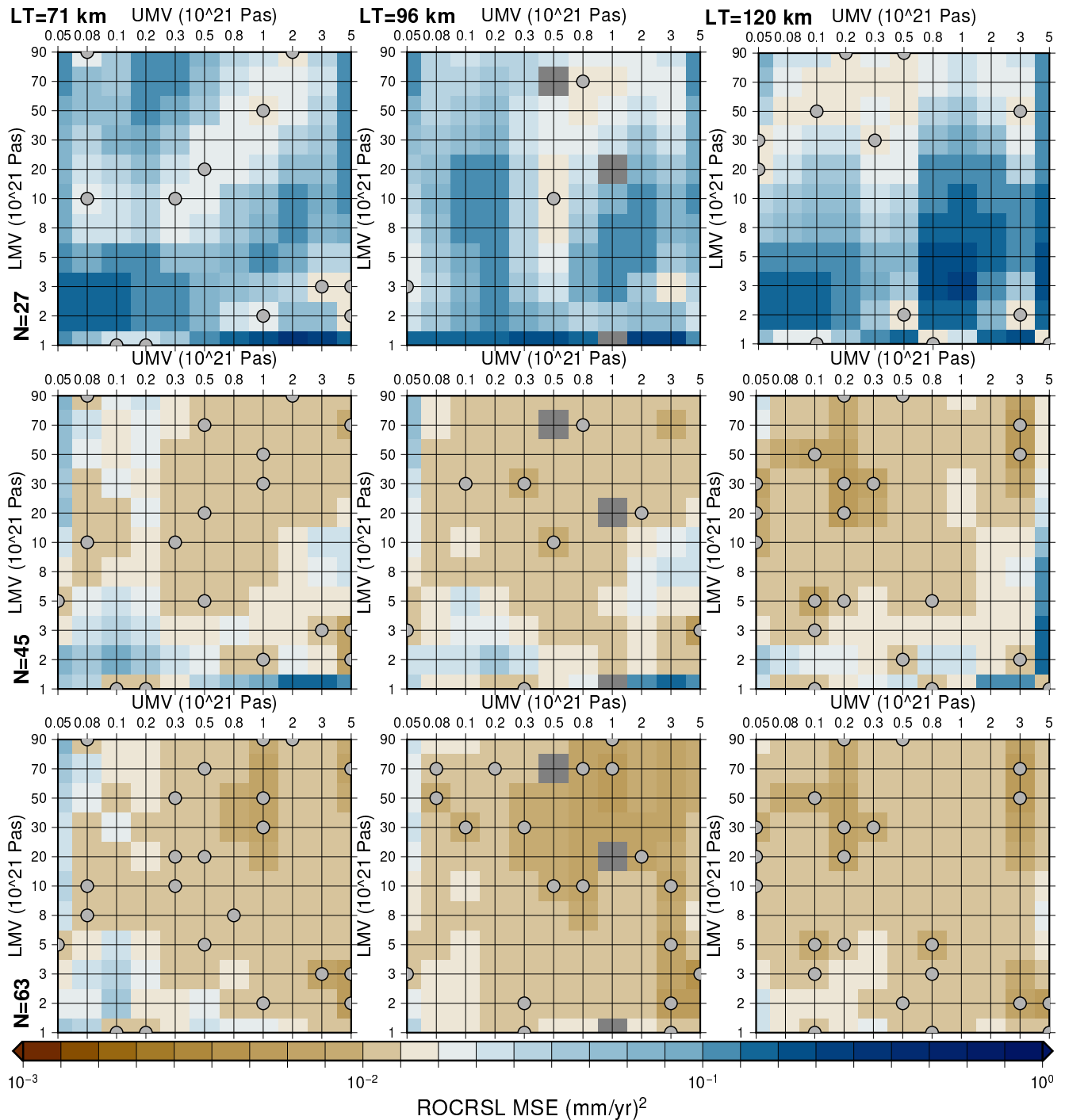


**Figure 2.** Plot shows the MSE (for all locations and time-steps) through parameter space (LT/UMV/LMV) for input training datasets with N=27 (top row), 45 (middle row), and 63 (bottom row) for the S40RTS+LR18 ROC RSL ANN. Parameter vectors included in the training dataset are indicated by grey circles. Columns give results for the three values of global-mean elastic lithosphere thickness: 71 km (left), 96 km (middle), 120 km (right). Note that results which are anomalous and were affected by technical issues for specific ensemble members are rendered here in grey.

285 contour in Fig 3) is problematic, as the emulator:model anomaly does not decrease with the same spatial pattern as the RSL  
field itself (although it does broadly share the same spatial pattern), thus there is a region where the anomaly is comparable to  
the RSL field itself. The spatial distribution of the emulator:model anomaly for RSL does not have a clear source, such as the  
shear-wave velocity anomaly from S40RTS or lithosphere thickness (as shown in Fig. 1). However, it is important to note that  
the sub-lithosphere (lateral) viscosity variations change with depth and so the patterns shown are only representative within  
290 limited depth ranges. The magnitude of the pattern scales with that of RSL, and so the ice-loading history is one controlling  
factor.

To complement Fig. 3, we also provide plots of the predicted RSL time series for the emulated and model-predicted output  
(and the difference) in Fig. 5. Examining the timeseries data in Fig. 5, we obtain similar findings to those of Fig. 2 in that the  
emulator:model misfit decreases as the number of parameter vectors in the training dataset increases in most locations (e.g.,  
295 there is a decrease in performance when N is increased from 45 to 63 at the Hudson Bay locality). This result is generally  
found across ice covered/near-field, intermediate-field, and far-field regions. The intermediate-field (e.g., Northern South-  
Carolina) is the most difficult portion of the field to emulate. The results show that  $\approx 45$  training members are generally  
sufficient to reproduce RSL using 3D Earth models for the ice covered/near field, intermediate, and far field regions shown  
here. Examination of results using fewer training members (N = 18, not shown) also indicates that fewer training members  
300 may be required to produce acceptable results for regions with greater density of training data (e.g., ice-covered regions).  
For the N = 18 case, misfits for Hudson's Bay are of the same order misfit compared to the N = 45 case. We note that, site  
depending, the difference in predicted RSL between the emulator and the Seakon results is generally small (i.e., of the same  
scale as proxy-data uncertainties) during the Holocene, the time interval for which the majority of RSL data exist. Although the  
aims and methods of this study are quite different to those in Lin et al. (2023), the RSL emulator errors obtained are broadly  
305 similar (e.g., compare our results for Hudson Bay and Barbados to, respectively, those in Fig. 2 (d & e) in Lin et al., 2023).

When examining the emulator:model differences (or anomalies) for contemporary uplift rates we find this method to be less  
accurate in comparison to RSL. The anomalies are generally of the same order of magnitude as the total modelled uplift rates  
for most regions (Figs. 4 and S7). However, the overall MSE results (e.g., as shown for ROC RSL in Fig. 2) are comparable  
when examined over the whole spatio-temporal dataset and so performance comparable to that for RSL is obtained for earlier  
310 time intervals (e.g., 10 ka; Fig. S8). The spatial distribution of the emulator:model anomaly for present day ROC of RAD more  
closely follows the overall distribution of the 3D Earth model's uplift field compared to the RSL results. While not investigated  
here, we propose the poorer results for this model output are a result of the input vector construction, specifically the way the  
ice sheet history is encoded. The ice sheet history comprises over half of the input vector to the ANN and predictions of the  
3D-SS uplift difference have no change in ice sheet history within the time range used to emulate ROC of RAD at present day  
315 (previous 4 time steps; for ICE-6G these are 0.5, 1.0, 1.5, and 2.0 ka). That is, at present day, the ANN has no information to  
distinguish a near-field location from a far-field location when considering the input ice history data. Restricting the training  
data input to the ANNs, or providing alternate ice history information (e.g., maximum ice thickness at that location within the  
last 10 ka) may provide greater ANN accuracy. Given the relatively low accuracy of our results for contemporary uplift rates  
we do not conduct data:model comparisons in Sect. 3.2.

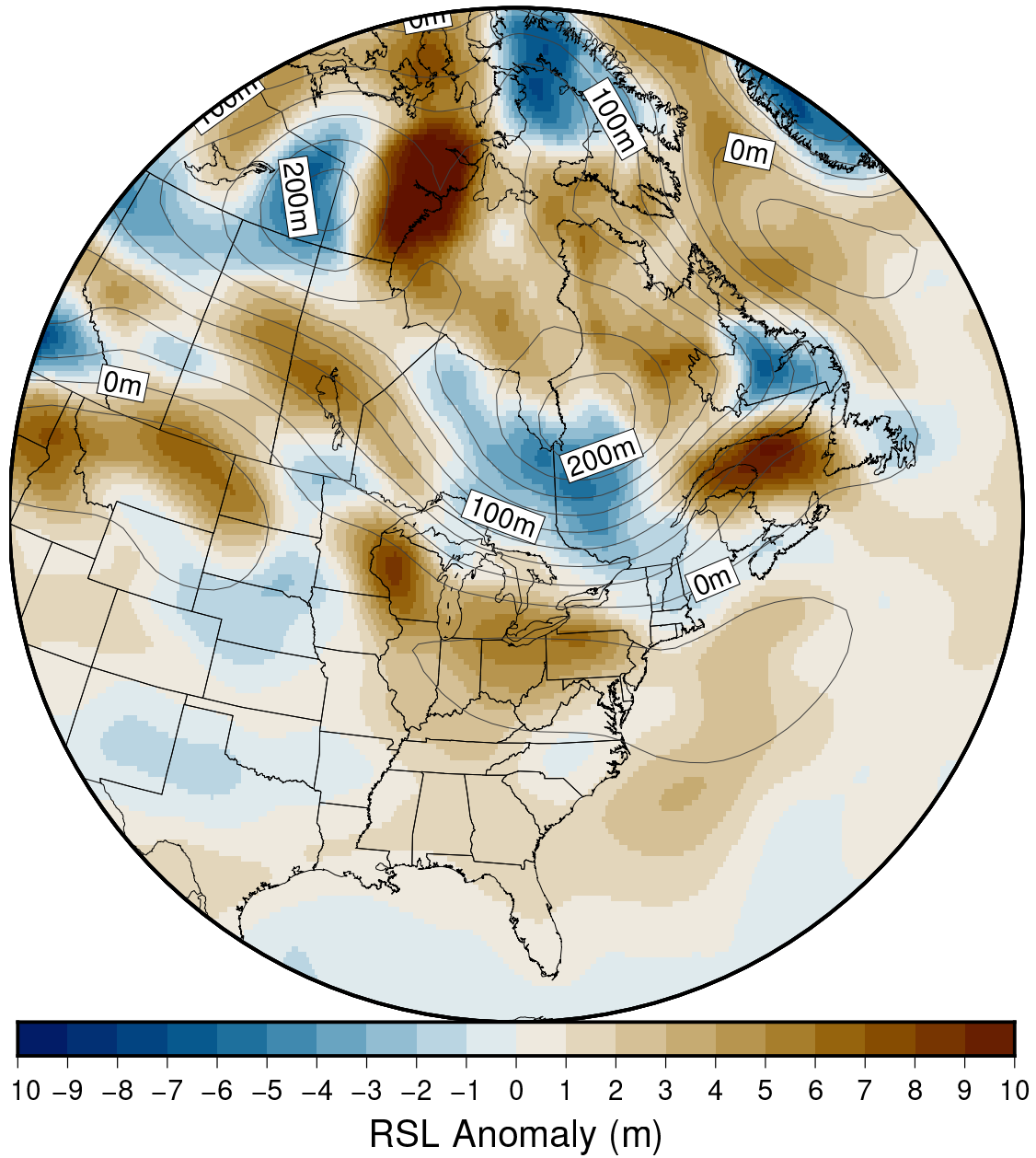


**Figure 3.** RSL anomaly: emulated RSL field minus explicit (3D-SS Seakon + NMSS) RSL field for the S40RTS+LR18 case, at 10 ka. Contours denote the RSL field (from the explicit case) in 25 m increments. The Earth model parameter vector used to generate these results is that with the median MSE, calculated for all spatio-temporal data, for the  $N = 45$  case. A global map of the same field is shown in Fig. S6

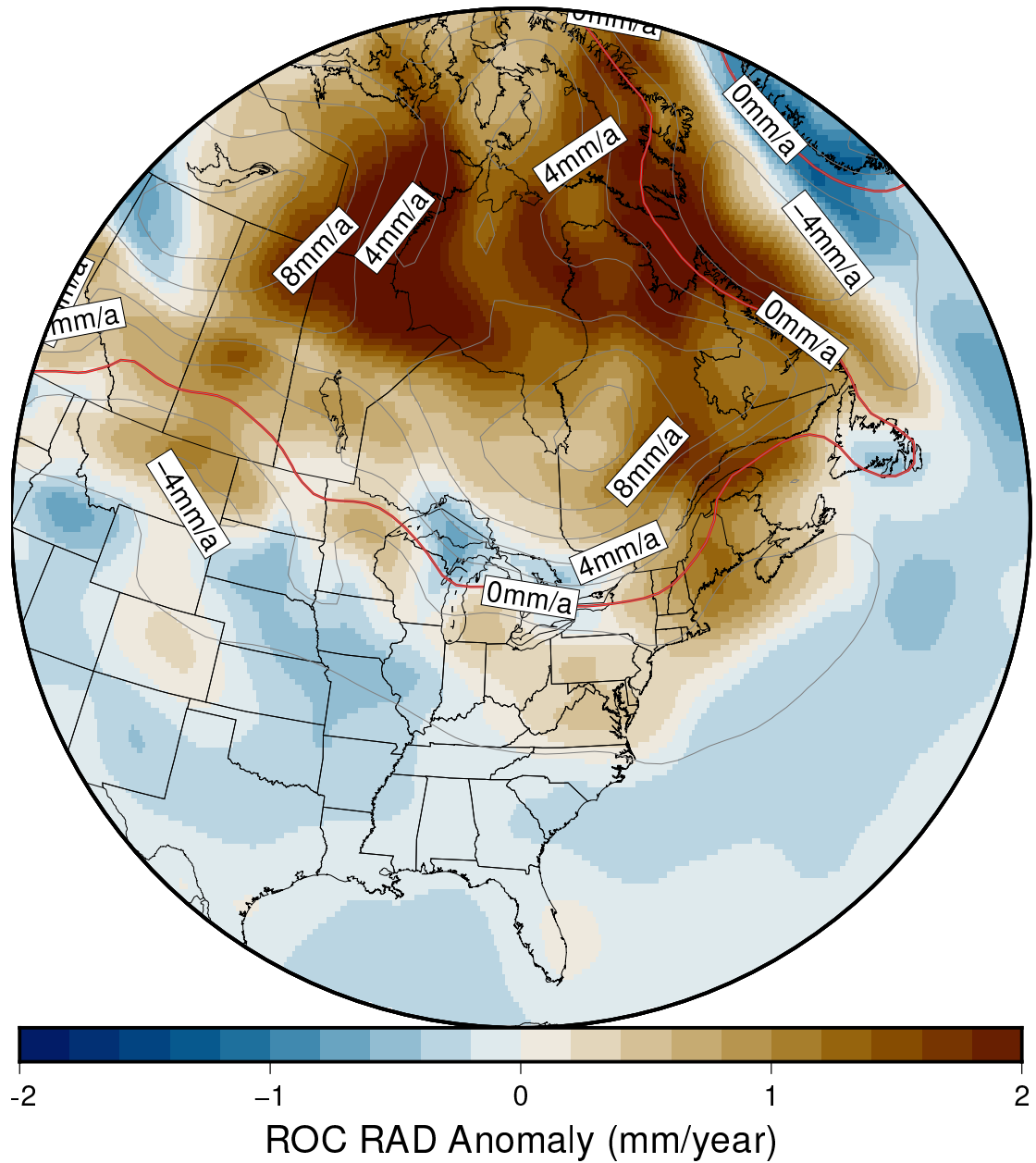


**Figure 4.** Emulated RAD field minus explicit (3D-SS Seakon + NMSS) field for the S40RTS+LR18 case at present day. Contours denote the total, modelled ROC RAD field (from the explicit case) in 2mm/yr increments; the red line denotes the 0mm/yr contour. The parameter vector plotted is that with the median MSE, calculated for all spatio-temporal data, for the  $N = 45$  ANN. A global map of the same field is shown in Fig. S7, and an equivalent map but for 10 ka is shown in Fig. S8.

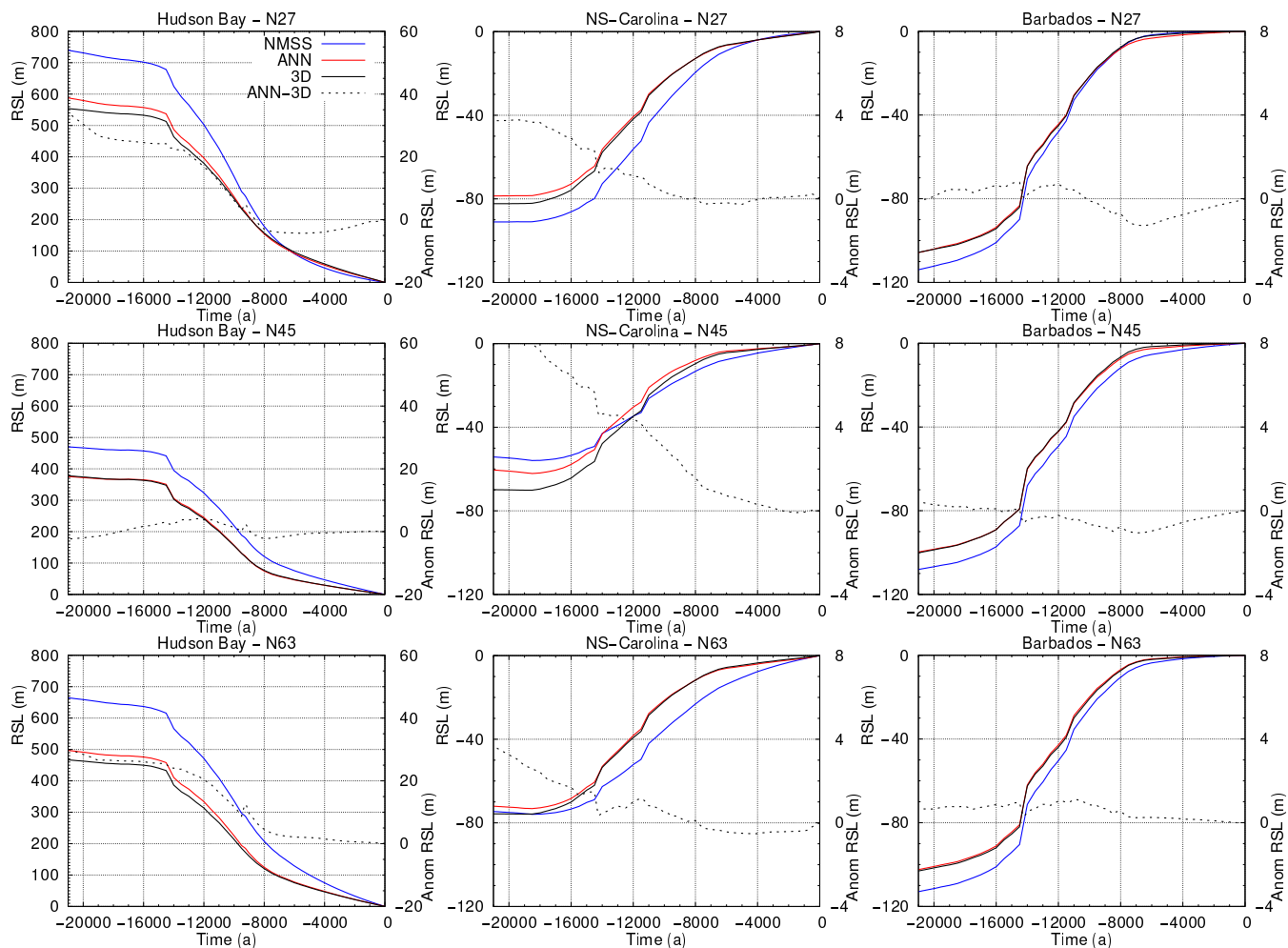


**Figure 5.** RSL timeseries for near- (Hudson Bay), intermediate- (Northern S-Carolina), and far-field (Barbados) locations, for the  $N=27$ , 45 and 63 ANN training sets. RSL curves are computed using the parameter vector corresponding to the median MSE for each validation ensemble. As the parameter vector for the mean MSE generally varies with  $N$ , the resulting RSL curves also change.

320 Comparing the above results to those for the semi-3D Earth model case, i.e., S40RTS with a SS lithosphere, we find similar amplitudes of emulator:model misfit with respect to contemporary uplift rates. The emulator:model misfit for RSL is generally smaller for the same number of training parameter vectors for this simpler Earth model - of particular note is that performance within intermediate-field locations is improved (see Fig. S9). Without exploring additional 3D Earth models we cannot conclude if this feature is a result of considering a simpler Earth model which does not incorporate the spatially variable elastic lithosphere, or a limitation of our methodology (e.g., network training or architecture). Despite this, of the configurations tested  
325 here, we find similar numbers of parameter vectors are required in the training dataset to obtain usable accuracy even for this simpler 3D Earth model.

Overall, we are able to successfully reproduce the influence of 3D Earth structure using ANNs trained using 45, or more, parameter vectors (out of a total of 330 for the LT/UMV/LMV values considered here) when considering past RSL and uplift  
330 rates. However, model:emulator misfits are generally of the same order of magnitude of the uplift and RSL rate field when considering contemporary values. As such, the emulator developed here is of limited utility for comparisons to contemporary uplift and RSL rates derived from geodetic data.

Several logical extensions to the methodology applied here became apparent over the course of this investigation. The first extension would be to implement a probabilistic Bayesian artificial neural network (BANNs, e.g. as described in Jospin et al.,  
335 2022). A BANN can provide estimates regarding the accuracy of a given prediction. Given that any error in the ROC of RSL or RAD propagates throughout the whole prediction (with respect to time), this information could be used to potentially reduce emulator:model misfits (e.g., via a cut-off where the ANN is not employed for a given prediction if the prediction confidence were too low). The second extension would be to include a parameter, or multiple parameters, in the inputs to the ANNs such that some information about the lateral Earth structure is encoded into the networks (e.g., scaling from seismic  
340 velocity anomaly to viscosity). This would allow evaluation across multiple realizations of lateral Earth structures without the need for separately trained datasets as was conducted in this investigation. The final extension would be to train the ANNs on multiple ice sheet histories in order to generalize their predictions across variations of this input parameter (Lin et al., 2023). Doing so requires no changes to the ANN or training data construction, simply conducting and processing additional Seakon simulations with multiple ice sheet histories. A brief exploration, not shown here, using the ANNs trained on the ICE6G ice  
345 sheet history to emulate model output corresponding with the ANU ice sheet reconstruction (Lambeck et al., 2014) resulted in large emulator:model RSL differences. This initial test underscores the need to train on multiple ice histories to produce more accurate results. Clearly, this would represent a challenge for the 3D case due to the computational inefficiency of the forward model.

### 3.2 Use of Emulator to Identify Optimal SS Viscosity Model

350 The emulator (i.e., the ANNs in combination with the NMSS model) is used here to examine the effects of imposing 3D viscosity variations, specifically those from the S40RTS+LR18 configuration, on reconstructions of RSL and associated inferences of Earth structure. The ANNs were trained using 45 parameter vectors, as identified in Sect. 3.1, to provide a balance between computational expense and accuracy. As part of the validation process for the emulator and to assess the scale of impacts re-



sulting from emulator:model differences, we calculate the proxy-data misfit values (Sect. 2.4) for the RSL database described in Sect. 2.4 for three different sources of model output: the NMSS model, the NMSS model combined with emulated 3D-SS output, and the NMSS model combined with explicit 3D-SS Seakon output. The choice of combining NMSS model output with the emulated 3D-SS output is an end-goal of the workflow, and we note that the SS Seakon output is, for the purposes of calculating the misfit, equivalent to that of the NMSS model. The results of these calculations, considering the total misfit (i.e., all RSL proxy data types), are shown in Fig. 6. Misfit values for SLIPS, limiting data, and all data are shown in Fig. S10 for the explicit (3D-SS+NMSS) output, with comparable misfit plots for the emulator output in Fig. S11 and the NMSS model output in Fig. S12. These results indicate that the total misfit values are dominated by the SLIPs and marine limiting data for each of three cases of model output.

The misfit results for the NMSS model runs are used as a baseline (or reference) for the two cases that include the influence of lateral Earth structure (modelled via Seakon or emulated via the ANNs). Comparing the results in the bottom two rows of Fig. 6 to those in the top row, we find that the emulator largely captures the impact of 3D viscosity structure on the misfit values but does not result in values that are indistinguishable with those determined from the explicit output. The emulated results are, upon visual inspection, more similar to the explicit results than the NMSS results alone. To quantify the effectiveness of the emulator across the entirety of the LT/UMV/LMV parameter space we use the MSE of the proxy-data:model misfit between the emulator and the explicit data, and the emulator and the NMSS data. That is, the emulator:NMSS MSE for SLIP data is,

$$\text{MSE}_{\text{emulator:NMSS}} = \frac{1}{n_{\text{LT}}n_{\text{UMV}}n_{\text{LMV}}} \sum_{\text{LT}=1}^{n_{\text{LT}}} \sum_{\text{UMV}=1}^{n_{\text{UMV}}} \sum_{\text{LMV}=1}^{n_{\text{LMV}}} \left( \delta_{\text{SLIP}}^{\text{emulator}}(\text{LT}, \text{UMV}, \text{LMV}) - \delta_{\text{SLIP}}^{\text{NMSS}}(\text{LT}, \text{UMV}, \text{LMV}) \right)^2 \quad (3)$$

where  $n_{\text{LT}}, n_{\text{UMV}}, n_{\text{LMV}}$  are, respectively, the number of LT, UMV, and LMV values in the explored parameter space, and  $\delta_{\text{SLIP}}^{\text{emulator}}, \delta_{\text{SLIP}}^{\text{NMSS}}$  are the SLIP misfit values as described in Sect. 2.4 for the emulator and NMSS data respectively. The MSE provides a metric which allows for comparison of the calculated proxy-data:model misfits for the emulator, NMSS, and the explicit results. In the ideal case of the misfits calculated using the emulator being identical to those from the explicit data the emulator:explicit MSE would be zero. MSE values for the SLIP data demonstrate that the emulator misfits are closer to those of the explicit model ( $\text{MSE}_{\text{SLIP}} = 0.74 \times 10^{-3}$ ) than the NMSS model ( $\text{MSE}_{\text{SLIP}} = 7.11 \times 10^{-3}$ ) which can also be concluded from Fig. 6.

Upon dividing the RSL dataset into the three regional subsets: the Canadian Arctic-Atlantic Coast (CAAC, Vacchi et al., 2018), the US-East Coast (USEC, Engelhart and Horton, 2012), and the US Gulf Coast (USGC, Hijma et al., 2015; Love et al., 2016), we find similar results (Figs. S13, S14, and S15) to those for the total database. Overall, the proxy-data:model misfits calculated using the output of the emulator are more like the explicit results than the NMSS results alone. This result is obtained both visually and when considering the MSE values for the emulator:explicit and emulator:NMSS misfits. Since the emulator has more difficulty in reproducing the influence of lateral Earth structure in the intermediate field, for  $N = 45$ , compared to near- and far-field locations (Fig. 5), it is interesting to compare the results for the USEC database (intermediate field) to the other two. For both the near-field CAAC database and the relatively distant USGC database, the MSE of the emulator:explicit misfit results are one to two orders of magnitude smaller than the emulator:NMSS misfit. In comparison, for

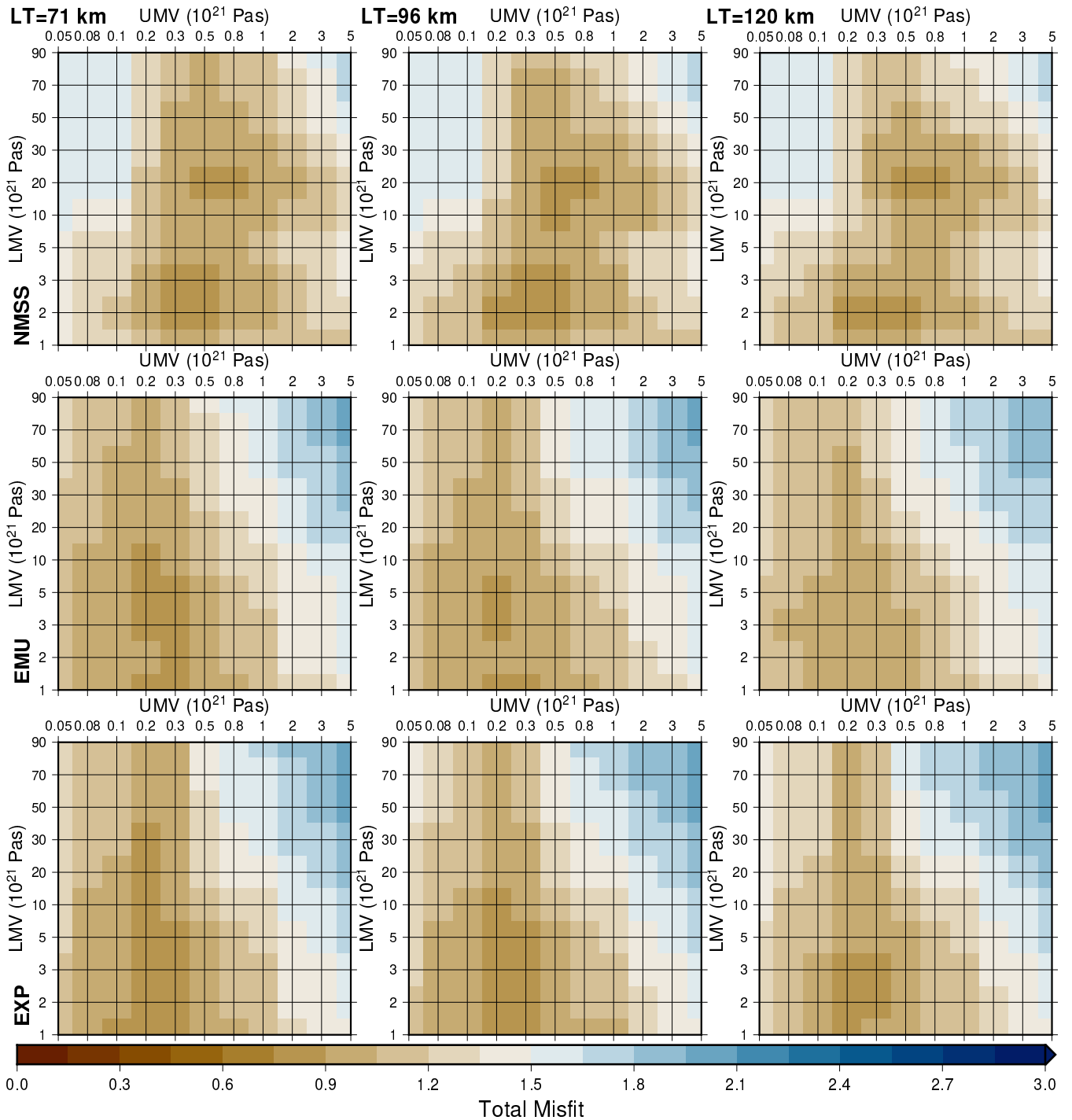


**Figure 6.** Proxy-data: model misfit using the RSL database (Sect. 2.4) for the NMSS model (top row), the emulator (EMU, middle row), and the explicit 3D-SS RSL output from Seakon added onto the NMSS RSL output (EXP, bottom row). Misfit varies as a function of global mean lithosphere thickness from left to right. Results are for the S40RTS+LR18 3D model configuration.

the intermediate-field USEC database, the MSE of the emulator:explicit misfit results are the same order of magnitude as the emulator:NMSS misfit results.

390 The misfit data presented in Fig. 6 and Table 1 demonstrate that the emulator, as employed here, is successful at reproducing the region in the LT/UMV/LMV parameter space which produces the lowest proxy-data:model misfits, and reproducing the relative values of proxy-data:model misfits throughout the parameter space. For the CAAC subset, the use of the emulator results in a parameter vector with minimum misfit that is either the same or within 2 parameter value increments (with respect to the evaluated LT/UMV/LMV values) of the explicitly derived minimum misfit parameters. This accuracy is also obtained when considering the combined dataset. For all the databases examined, the parameter vector which produces the minimum misfit obtained by emulation is closer (in parameter space) to the explicit 3D-SS+NMSS case than the NMSS case. As such, using the emulator we are able to identify the region of LT/UMV/LMV parameter space that optimizes the fit for a given lateral structure model (S40RTS+LR18). For example, the sub-region defined by UMV ( $0.1 - 0.3 \times 10^{21} \text{ Pa} \cdot \text{s}$ ) and LMV ( $1 - 10 \times 10^{21} \text{ Pa} \cdot \text{s}$ ) (Fig. 6). This smaller region of parameter space could then be explored using the explicit model to more accurately determine the optimal parameter vectors.

400 Previous work has typically used spatially confined, regional-scale analyses to mitigate the influence of lateral Earth structure when using the assumption of spherical symmetry in the GIA model (e.g., Love et al., 2016; Yousefi et al., 2018). The expectation is that as spatial scales grow larger, those Earth models which incorporate 3D structure will outperform SS Earth models. Examining the misfit results in Fig. 6 and Table 1, we do not find the 3D Earth model considered here consistently outperforms SS Earth models on large spatial scales. As noted in the Introduction, this has been demonstrated in many past studies (e.g., Steffen et al., 2006; Spada et al., 2006; van der Wal et al., 2013; Li et al., 2018). For some cases in our results, e.g.  $\delta_{SLIP}$  for the US Gulf Coast, the 3D model produces a lower misfit in comparison to the SS model. However, that the 3D model results in lower proxy-data:model misfits on regional scales is expected given we are effectively adding, at least, two additional parameters to the model to find the minimum proxy-data:model misfit. Despite these findings, there are features in Fig. 6 which can be used to guide future investigations, e.g., the distribution and number of minima throughout the parameter space is different between the 3D and SS Earth models. The region of minimum misfit for the 3D Earth model is fairly broad but defines a single minimum in the explored parameter space, rather than two distinct but relatively localized minima determined using the SS Earth models. There is a shift in the preferred UMV: for example, the UMV for the minimum misfit Earth model for the USEC  $\delta_{SLIP}$  is  $3 \times 10^{21} \text{ Pa} \cdot \text{s}$  for the SS Earth model compared to  $0.3 \times 10^{21} \text{ Pa} \cdot \text{s}$  for the 3D Earth model. This shows that radial viscosity structure inferred using a SS model can be significantly biased (e.g., Lau et al., 2018; Li et al., 415 2022).

Overall, the SS Earth models still result in the lowest proxy-data:model misfits for the combined NA dataset. This suggests that our inputs to the 3D GIA model are incorrect. Given that we have investigated (for this study) only a single realization of lateral variability (to impose on a background SS Earth model) and a single ice sheet reconstruction, it is not possible to determine which dominates (if any) in producing the higher than expected misfit results. Since ice sheet reconstructions (like 420 ICE-6G) are developed assuming a SS GIA model, it is not surprising that the SS Earth models outperform or give similar quality of fit to the 3D Earth models in ice covered areas (e.g., van der Wal et al., 2013; Li et al., 2020). This is also the reason

why the optimum LT/UMV/LMV parameter set inferred here is a good approximation to the radial viscosity model assumed when constructing ICE-6G (i.e., VM5a).

An important aim of future work will be to develop ice sheet models that are consistent with inferred 3D Earth structure. Previous investigations (e.g., Gomez et al., 2018; van Calcar et al., 2023) demonstrate that coupling 3D Earth models to a dynamical ice sheet model applied to Antarctica results in considerable local ice thickness changes while not significantly impacting ice sheet volume when compared to results for a SS Earth model. These more consistent 3D Earth-ice model pairings would hopefully result in improved fits to GIA-related data sets in near-field regions (compared to the SS Earth-ice model fits). In this regard, one potentially important extension of this work is to consider developing an ANN that can emulate results with different ice sheet histories. (Lin et al., 2023) have demonstrated that good results can be obtained with a 1D Earth model and so there is potential to consider the case of a 3D Earth model. Again, a key challenge will be to obtain useful results in near-field regions with a relatively small training set. If successful, such an emulator could be used in coupled GIA-ice sheet modelling to include the effect of lateral variations in Earth structure. This would result in computation times that are equivalent to those for coupled SS GIA-ice sheet models (i.e.,  $\approx 10000$  times more efficient vs. the reduced resolution configuration used in this study).

		$\delta_{SLIP}$	$\delta_{ML}$	$\delta_{TL}$	$\delta_{Total}$
CAAC					
NMSS	Minimum Misfit	0.075	0.021	0.108	0.383
	LT/UMV/LMV	96/0.30/2	46/0.80/5	120/0.80/90	71/0.50/2
EMU	Minimum Misfit	0.184	0.334	0.564	0.944
	LT/UMV/LMV	71/0.20/1	71/0.20/2	96/0.30/90	71/0.20/1
EXP	Minimum Misfit	0.188	0.286	0.566	0.885
	LT/UMV/LMV	71/0.20/2	71/0.30/2	120/0.80/90	71/0.20/1
US East Coast					
NMSS	Minimum Misfit	0.07	0	0	0.154
	LT/UMV/LMV	71/3.00/50			71/3.00/90
EMU	Minimum Misfit	0.064	0	0	0.125
	LT/UMV/LMV	71/0.50/50			120/0.50/30
EXP	Minimum Misfit	0.068	0	0	0.130
	LT/UMV/LMV	71/0.30/3			120/0.80/50
US Gulf Coast					
NMSS	Minimum Misfit	0.164	0.188	1.688	1.613
	LT/UMV/LMV	71/1.00/20	120/1.00/90	120/0.08/90	71/1.00/20
EMU	Minimum Misfit	0.149	0.179	1.959	1.619
	LT/UMV/LMV	96/0.05/3	120/0.80/90	120/0.08/90	96/0.05/3
EXP	Minimum Misfit	0.156	0.164	1.830	1.631
	LT/UMV/LMV	120/0.05/3	120/0.80/90	120/0.08/90	71/0.80/5
Combined NA					
NMSS	Minimum Misfit	0.091	0.288	0.977	0.823
	LT/UMV/LMV	96/0.30/2	46/0.50/2	71/0.10/90	96/0.30/2
EMU	Minimum Misfit	0.111	0.302	1.003	0.836
	LT/UMV/LMV	71/0.20/5	71/0.30/3	71/0.10/90	71/0.20/1
EXP	Minimum Misfit	0.103	0.273	0.969	0.823
	LT/UMV/LMV	71/0.20/2	71/0.30/3	71/0.10/90	71/0.20/2

**Table 1.** Misfits for the Canadian Arctic-Atlantic Coast (Vacchi et al., 2018), US East Coast (Engelhart and Horton, 2012), and US Gulf Coast (Hijma et al., 2015; Love et al., 2016) RSL databases broken down into the contributing misfits for sea-level index points, marine & terrestrial limiting, and combined total as defined in Sect. 2.4. The lowest misfit for each of the data-types (i.e. SLIP, ML, TL, and total) and corresponding combination of SS lithospheric thickness(km), upper mantle viscosity( $\times 10^{21}$  Pa · s), and lower mantle viscosity( $\times 10^{21}$  Pa · s) are given for each region. Values are given for output generated using the NMSS, the emulator (ANN derived 3D-SS + NMSS), and explicit (Seakon 3D-SS + NMSS) cases. Note that LT/UMV/LMV values for misfits of zero in the limiting data columns for the USEC are not unique and thus left blank.

## 4 Conclusions

This study provides an initial “proof of concept” assessment of using ANNs to emulate the influence of lateral Earth structure on GIA model output. We used the Tensorflow software library to produce ANNs, implement an emulator, and test the effectiveness of the emulator using model output of past (deglacial) sea-level change and present-day vertical land motion from a 3D (Earth) GIA numerical model and a commonly used SS (Earth) GIA numerical model. Our goal is to test whether the emulator can accurately predict the difference in these outputs (i.e., RSL and uplift rates) for the 3D case relative to the SS case. We pursued this application for three realisations of (global) lateral Earth structure (S40RTS, S40RTS+LR18, Savani+LR18 Ritsema et al., 2010; Afonso et al., 2019; Auer et al., 2014) and a commonly used ice history model (ICE6G, Peltier et al., 2015; Roy and Peltier, 2017).

Our results indicate that the emulator:model differences, while not negligible, are of a scale such that useful predictions of deglacial RSL changes can be made. Evaluation of the emulator performance for deglacial RSL indicates that it is able to provide useful estimates of this field throughout the LT/UMV/LMV parameter space when trained on only  $\approx 15\%$  (45) of the parameter vectors considered (330 in total). In contrast, results for present-day vertical land motion are poorer, with emulator errors of similar order to the 3D minus SS model output. Better results for emulating vertical land motion were obtained for model time steps when ice was still present, suggesting that the performance of the emulator (for present-day rates) could be improved by modifying inputs provided to the ANNs with respect to the input ice history information (e.g., maximum ice thickness at that location within the last 10 ka, and/or a time history extending beyond the past 4 time steps). An important extension of this work is to consider different ice sheet models to determine if useful results can also be achieved for variations in this important GIA model parameter.

Given the relatively accurate results obtained for RSL, we applied the emulator in a proxy-data:model comparison exercise using RSL data distributed along North American coasts, from the Canadian Arctic to the US Gulf coast. The goals of this data:model comparison are two-fold: to determine if the emulator can produce accurate misfit values through the entire LT/UMV/LMV parameter space considered, and evaluate if the 3D Earth models can produce improved fits compared to the SS Earth models (for the chosen ice sheet and lateral Earth structure models). We find that the emulator is able to successfully reproduce the data:model misfit values such that generally the region of minimum misfit either overlaps the 3D GIA model results, or is within two increments in the parameter space. The emulator can, therefore, be used to more efficiently explore this aspect of the 3D Earth model parameter space. Furthermore, the parameter values that give best fits for 3D and SS models are quite different, supporting previous work that show inferences of radial viscosity structure can be significantly biased when assuming SS structure. Thus, future work on the application of ANNs to further explore the parameter space of 3D Earth models and ice sheet histories is required.

*Code and data availability.* Software for training the artificial neural networks, model network weights, and the various utilities which comprise the emulator/surrogate model are available in the supplemental materials via Zenodo (Love et al., 2023a) and are licensed under the GNU Public Licence (GPL) v3. Example datasets, to use as templates and testing, are also included in the supplemental materials. Training

data for the filtered datasets are available via Zenodo (Love et al., 2023b) and are licensed under the Creative Commons Attribution 4.0  
470 licence. Unfiltered training data is available only upon request due to the large file-sizes involved. Additional model output beyond the scope  
of the above availability statement may be available upon request. Source code for the GIA models used in this study are available from their  
corresponding developers.

*Competing interests.* The authors declare that no competing interests are present.

## 5 Author Contributions

475 RL, GAM, PA, and LT contributed to the design and analysis of the ANNs. RL, GAM, and SP contributed to analysis and  
discussion. RL conducted all simulations and data processing with assistance from KL. RL and GAM prepared the manuscript  
with contributions from all authors.

## 6 Acknowledgements

480 The authors would also like to thank those at the GNU and Fedora projects, Kernel.org, Tensorflow and in particular those  
responsible for GNU Parallel (Tange, 2011) whose software greatly sped up and streamlined the analysis in this work. This  
research was enabled in part by support provided by SciNet ([www.scinethpc.ca](http://www.scinethpc.ca)) and the Digital Research Alliance of Canada  
(formerly Compute Canada, <https://alliancecan.ca>) through the Rapid Access Service. RL, PA, SP, and GAM acknowledge  
funding support from the Natural Sciences and Engineering Research Council of Canada. LT acknowledges funding support  
from the PALMOD project.

## 485 References

- Abadi, M., Agarwal, A., Barham, P., et al.: TensorFlow: Large-Scale Machine Learning on Heterogeneous Systems, <https://www.tensorflow.org/>, 2015.
- Afonso, J. C., Salajegheh, F., Szwillus, W., Ebbing, J., and Gaina, C.: A global reference model of the lithosphere and upper mantle from joint inversion and analysis of multiple data sets, *Geophysical Journal International*, 217, 1602–1628, <https://doi.org/10.1093/gji/ggz094>,  
490 2019.
- Auer, L., Boschi, L., Becker, T. W., Nissen-Meyer, T., and Giardini, D.: Savani : A variable resolution whole-mantle model of anisotropic shear velocity variations based on multiple data sets, *Journal of Geophysical Research: Solid Earth*, 119, 3006–3034, <https://doi.org/10.1002/2013jb010773>, 2014.
- Austermann, J., Mitrovica, J. X., Latychev, K., and Milne, G. A.: Barbados-based estimate of ice volume at Last Glacial Maximum affected  
495 by subducted plate, *Nature Geoscience*, 6, 553–557, <https://doi.org/10.1038/ngeo1859>, 2013.
- Bagge, M., Klemann, V., Steinberger, B., Latinović, M., and Thomas, M.: Glacial-Isostatic Adjustment Models Using Geodynamically Constrained 3D Earth Structures, *Geochemistry, Geophysics, Geosystems*, 22, <https://doi.org/10.1029/2021gc009853>, 2021.
- Baril, A., Garrett, E., Milne, G., Gehrels, W., and Kelley, J.: Postglacial relative sea-level changes in the Gulf of Maine, USA: Database compilation, assessment and modelling, *Quaternary Science Reviews*, 306, 108 027, <https://doi.org/10.1016/j.quascirev.2023.108027>, 2023.
- 500 Caron, L., Métivier, L., Greff-Lefftz, M., Fleitout, L., and Rouby, H.: Inverting Glacial Isostatic Adjustment signal using Bayesian framework and two linearly relaxing rheologies, *Geophysical Journal International*, 209, 1126–1147, <https://doi.org/10.1093/gji/ggx083>, 2017.
- Chollet, F.: *Deep learning with Python*, Simon and Schuster, 2021.
- Cramer, F.: Scientific colour maps, <https://doi.org/10.5281/zenodo.8409685>, 2023.
- Crawford, O., Al-Attar, D., Tromp, J., Mitrovica, J. X., Austermann, J., and Lau, H. C. P.: Quantifying the sensitivity of post-glacial sea level  
505 change to laterally varying viscosity, *Geophysical Journal International*, 214, 1324–1363, <https://doi.org/10.1093/gji/ggy184>, 2018.
- Engelhart, S. E. and Horton, B. P.: Holocene sea level database for the Atlantic coast of the United States, *Quaternary Science Reviews*, 54, 12–25, <https://doi.org/10.1016/j.quascirev.2011.09.013>, 2012.
- Farrell, W. E. and Clark, J. A.: On Postglacial Sea Level, *Geophysical Journal of the Royal Astronomical Society*, 46, 647–667, <https://doi.org/10.1111/j.1365-246x.1976.tb01252.x>, 1976.
- 510 Gomez, N., Latychev, K., and Pollard, D.: A Coupled Ice Sheet–Sea Level Model Incorporating 3D Earth Structure: Variations in Antarctica during the Last Deglacial Retreat, *Journal of Climate*, 31, 4041–4054, <https://doi.org/10.1175/jcli-d-17-0352.1>, 2018.
- Hijma, M. P., Engelhart, S. E., Törnqvist, T. E., Horton, B. P., Hu, P., and Hill, D. F.: A protocol for a geological sea-level database, *Handbook of Sea-Level Research*, p. 536–553, <https://doi.org/10.1002/9781118452547.ch34>, 2015.
- Jospin, L. V., Laga, H., Boussaid, F., Buntine, W., and Bennamoun, M.: Hands-On Bayesian Neural Networks—A Tutorial for Deep Learning  
515 Users, *IEEE Computational Intelligence Magazine*, 17, 29–48, <https://doi.org/10.1109/mci.2022.3155327>, 2022.
- Karato, S.-i.: *Deformation of earth materials, An introduction to the rheology of Solid Earth*, 463, 2008.
- Kendall, R. A., Mitrovica, J. X., and Milne, G. A.: On post-glacial sea level - II. Numerical formulation and comparative results on spherically symmetric models, *Geophysical Journal International*, 161, 679–706, <https://doi.org/10.1111/j.1365-246x.2005.02553.x>, 2005.
- Klemann, V., Ivins, E. R., Martinec, Z., and Wolf, D.: Models of active glacial isostasy roofing warm subduction: Case of the South Patagonian  
520 Ice Field, *Journal of Geophysical Research*, 112, <https://doi.org/10.1029/2006jb004818>, 2007.



- Kuchar, J., Milne, G., and Latychev, K.: The importance of lateral Earth structure for North American glacial isostatic adjustment, *Earth and Planetary Science Letters*, 512, 236–245, <https://doi.org/10.1016/j.epsl.2019.01.046>, 2019.
- Lambeck, K., Rouby, H., Purcell, A., Sun, Y., and Sambridge, M.: Sea level and global ice volumes from the Last Glacial Maximum to the Holocene, *Proceedings of the National Academy of Sciences*, 111, 15 296–15 303, <https://doi.org/10.1073/pnas.1411762111>, 2014.
- 525 Latychev, K., Mitrovica, J. X., Tromp, J., Tamisiea, M. E., Komatitsch, D., and Christara, C. C.: Glacial isostatic adjustment on 3-D Earth models: a finite-volume formulation, *Geophysical Journal International*, 161, 421–444, <https://doi.org/10.1111/j.1365-246x.2005.02536.x>, 2005.
- Lau, H. C. P., Austermann, J., Mitrovica, J. X., Crawford, O., Al-Attar, D., and Latychev, K.: Inferences of Mantle Viscosity Based on Ice Age Data Sets: The Bias in Radial Viscosity Profiles Due to the Neglect of Laterally Heterogeneous Viscosity Structure, *Journal of Geophysical Research: Solid Earth*, 123, 7237–7252, <https://doi.org/10.1029/2018jb015740>, 2018.
- 530 Li, T., Wu, P., Steffen, H., and Wang, H.: In search of laterally heterogeneous viscosity models of glacial isostatic adjustment with the ICE-6G\_C global ice history model, *Geophysical Journal International*, 214, 1191–1205, <https://doi.org/10.1093/gji/ggy181>, 2018.
- Li, T., Wu, P., Wang, H., Steffen, H., Khan, N. S., Engelhart, S. E., Vacchi, M., Shaw, T. A., Peltier, W. R., and Horton, B. P.: Uncertainties of Glacial Isostatic Adjustment Model Predictions in North America Associated With 3D Structure, *Geophysical Research Letters*, 47, <https://doi.org/10.1029/2020gl087944>, 2020.
- 535 Li, T., Khan, N. S., Baranskaya, A. V., Shaw, T. A., Peltier, W. R., Stuhne, G. R., Wu, P., and Horton, B. P.: Influence of 3D Earth Structure on Glacial Isostatic Adjustment in the Russian Arctic, *Journal of Geophysical Research: Solid Earth*, 127, <https://doi.org/10.1029/2021jb023631>, 2022.
- Lin, Y., Whitehouse, P. L., Valentine, A. P., and Woodroffe, S. A.: GEORGIA: A Graph Neural Network Based EmulatOR for Glacial Isostatic Adjustment, *Geophysical Research Letters*, 50, <https://doi.org/10.1029/2023gl103672>, 2023.
- 540 Love, R., Milne, G. A., Tarasov, L., Engelhart, S. E., Hijma, M. P., Latychev, K., Horton, B. P., and Törnqvist, T. E.: The contribution of glacial isostatic adjustment to projections of sea-level change along the Atlantic and Gulf coasts of North America, *Earth's Future*, 4, 440–464, <https://doi.org/10.1002/2016ef000363>, 2016.
- Love, R., Milne, G. A., Ajourlou, P., Parang, S., Tarasov, L., and Latychev, K.: Supplemental Materials for A Fast Surrogate Model for 3D-Earth Glacial Isostatic Adjustment using Tensorflow (v2.8.10) Artificial Neural Networks, <https://doi.org/10.5281/zenodo.10045462>, 2023a.
- 545 Love, R., Milne, G. A., Ajourlou, P., Parang, S., Tarasov, L., and Latychev, K.: Input Data for A Fast Surrogate Model for 3D-Earth Glacial Isostatic Adjustment using Tensorflow (v2.8.10) Artificial Neural Networks, <https://doi.org/10.5281/zenodo.10042047>, 2023b.
- Milne, G. A.: Glacial isostatic adjustment, *Handbook of Sea-Level Research*, p. 419–437, <https://doi.org/10.1002/9781118452547.ch28>, 2015.
- 550 Milne, G. A. and Mitrovica, J. X.: Postglacial sea-level change on a rotating Earth, *Geophysical Journal International*, 133, 1–19, <https://doi.org/10.1046/j.1365-246x.1998.1331455.x>, 1998.
- Mitrovica, J. X. and Milne, G. A.: On post-glacial sea level: I. General theory, *Geophysical Journal International*, 154, 253–267, <https://doi.org/10.1046/j.1365-246x.2003.01942.x>, 2003.
- 555 Mitrovica, J. X. and Peltier, W. R.: On postglacial geoid subsidence over the equatorial oceans, *Journal of Geophysical Research: Solid Earth*, 96, 20 053–20 071, <https://doi.org/10.1029/91jb01284>, 1991.
- Mitrovica, J. X. and Peltier, W. R.: A comparison of methods for the inversion of viscoelastic relaxation spectra, *Geophysical Journal International*, 108, 410–414, <https://doi.org/10.1111/j.1365-246x.1992.tb04623.x>, 1992.

- Mitrovica, J. X., Wahr, J., Matsuyama, I., and Paulson, A.: The rotational stability of an ice-age earth, *Geophysical Journal International*, 161, 491–506, <https://doi.org/10.1111/j.1365-246x.2005.02609.x>, 2005.
- 560 Pan, L., Milne, G. A., Latychev, K., Goldberg, S. L., Austermann, J., Hoggard, M. J., and Mitrovica, J. X.: The influence of lateral Earth structure on inferences of global ice volume during the Last Glacial Maximum, *Quaternary Science Reviews*, 290, 107–144, <https://doi.org/10.1016/j.quascirev.2022.107644>, 2022.
- Paulson, A., Zhong, S., and Wahr, J.: Modelling post-glacial rebound with lateral viscosity variations, *Geophysical Journal International*, 163, 357–371, <https://doi.org/10.1111/j.1365-246x.2005.02645.x>, 2005.
- 565 Paulson, A., Zhong, S., and Wahr, J.: Inference of mantle viscosity from GRACE and relative sea level data, *Geophysical Journal International*, 171, 497–508, <https://doi.org/10.1111/j.1365-246x.2007.03556.x>, 2007.
- Peltier, W. R.: The impulse response of a Maxwell Earth, *Reviews of Geophysics*, 12, 649, <https://doi.org/10.1029/rg012i004p00649>, 1974.
- Peltier, W. R.: Glacial-Isostatic Adjustment-II. The Inverse Problem, *Geophysical Journal of the Royal Astronomical Society*, 46, 669–705, <https://doi.org/10.1111/j.1365-246x.1976.tb01253.x>, 1976.
- 570 Peltier, W. R., Argus, D. F., and Drummond, R.: Space geodesy constrains ice age terminal deglaciation: The global ICE6GC (VM5a) model, *Journal of Geophysical Research: Solid Earth*, 120, 450–487, <https://doi.org/10.1002/2014jb011176>, 2015.
- Powell, E. M., Pan, L., Hoggard, M. J., Latychev, K., Gomez, N., Austermann, J., and Mitrovica, J. X.: The impact of 3-D Earth structure on far-field sea level following interglacial West Antarctic Ice Sheet collapse, *Quaternary Science Reviews*, 273, 107–126, <https://doi.org/10.1016/j.quascirev.2021.107256>, 2021.
- 575 Ritsema, J., Deuss, A., van Heijst, H. J., and Woodhouse, J. H.: S40RTS: a degree-40 shear-velocity model for the mantle from new Rayleigh wave dispersion, teleseismic traveltime and normal-mode splitting function measurements, *Geophysical Journal International*, 184, 1223–1236, <https://doi.org/10.1111/j.1365-246x.2010.04884.x>, 2010.
- Roy, K. and Peltier, W.: Space-geodetic and water level gauge constraints on continental uplift and tilting over North America: regional convergence of the ICE-6G\_C (VM5a/VM6) models, *Geophysical Journal International*, 210, 1115–1142, <https://doi.org/10.1093/gji/ggx156>, 2017.
- 580 Sellevold, R. and Vizcaino, M.: First Application of Artificial Neural Networks to Estimate 21st Century Greenland Ice Sheet Surface Melt, *Geophysical Research Letters*, 48, <https://doi.org/10.1029/2021gl092449>, 2021.
- Shepherd, A., Ivins, E. R., A., G., Barletta, V. R., Bentley, M. J., Bettadpur, S., Briggs, K. H., Bromwich, D. H., Forsberg, R., Galin, N., Horwath, M., Jacobs, S., Joughin, I., King, M. A., Lenaerts, J. T. M., Li, J., Ligtenberg, S. R. M., Luckman, A., Luthcke, S. B., McMillan, M., Meister, R., Milne, G., Mouginot, J., Muir, A., Nicolas, J. P., Paden, J., Payne, A. J., Pritchard, H., Rignot, E., Rott, H., Sørensen, L. S., Scambos, T. A., Scheuchl, B., Schrama, E. J. O., Smith, B., Sundal, A. V., van Angelen, J. H., van de Berg, W. J., van den Broeke, M. R., Vaughan, D. G., Velicogna, I., Wahr, J., Whitehouse, P. L., Wingham, D. J., Yi, D., Young, D., and Zwally, H. J.: A Reconciled Estimate of Ice-Sheet Mass Balance, *Science*, 338, 1183–1189, <https://doi.org/10.1126/science.1228102>, 2012.
- 585 Spada, G.: Glacial Isostatic Adjustment and Contemporary Sea Level Rise: An Overview, pp. 155–187, Springer International Publishing, [https://doi.org/10.1007/978-3-319-56490-6\\_8](https://doi.org/10.1007/978-3-319-56490-6_8), 2017.
- Spada, G., Antonioli, A., Cianetti, S., and Giunchi, C.: Glacial isostatic adjustment and relative sea-level changes: the role of lithospheric and upper mantle heterogeneities in a 3-D spherical Earth, *Geophysical Journal International*, 165, 692–702, <https://doi.org/10.1111/j.1365-246x.2006.02969.x>, 2006.
- 595 Steffen, H. and Kaufmann, G.: Glacial isostatic adjustment of Scandinavia and northwestern Europe and the radial viscosity structure of the Earth's mantle, *Geophysical Journal International*, 163, 801–812, <https://doi.org/10.1111/j.1365-246x.2005.02740.x>, 2005.

- Steffen, H., Kaufmann, G., and Wu, P.: Three-dimensional finite-element modeling of the glacial isostatic adjustment in Fennoscandia, *Earth and Planetary Science Letters*, 250, 358–375, <https://doi.org/10.1016/j.epsl.2006.08.003>, 2006.
- Steffen, H., Denker, H., and Müller, J.: Glacial isostatic adjustment in Fennoscandia from GRACE data and comparison with geodynamical models, *Journal of Geodynamics*, 46, 155–164, <https://doi.org/10.1016/j.jog.2008.03.002>, 2008.
- 600 Tange, O.: GNU Parallel - The Command-Line Power Tool, *login: The USENIX Magazine*, 36, 42–47, <http://www.gnu.org/s/parallel>, 2011.
- Tarasov, L., Dyke, A. S., Neal, R. M., and Peltier, W.: A data-calibrated distribution of deglacial chronologies for the North American ice complex from glaciological modeling, *Earth and Planetary Science Letters*, 315–316, 30 – 40, <https://doi.org/http://dx.doi.org/10.1016/j.epsl.2011.09.010>, sea Level and Ice Sheet Evolution: A {PALSEA} Special Edition, 2012.
- 605 Vacchi, M., Engelhart, S. E., Nikitina, D., et al.: Postglacial relative sea-level histories along the eastern Canadian coastline, *QSR*, 201, 124–146, <https://doi.org/10.1016/j.quascirev.2018.09.043>, 2018.
- van Calcar, C. J., van de Wal, R. S. W., Blank, B., de Boer, B., and van der Wal, W.: Simulation of a fully coupled 3D glacial isostatic adjustment – ice sheet model for the Antarctic ice sheet over a glacial cycle, *Geoscientific Model Development*, 16, 5473–5492, <https://doi.org/10.5194/gmd-16-5473-2023>, 2023.
- 610 van der Wal, W., Wu, P., Sideris, M. G., and Shum, C.: Use of GRACE determined secular gravity rates for glacial isostatic adjustment studies in North-America, *Journal of Geodynamics*, 46, 144–154, <https://doi.org/10.1016/j.jog.2008.03.007>, 2008.
- van der Wal, W., Barnhoorn, A., Stocchi, P., Gradmann, S., Wu, P., Drury, M., and Vermeersen, B.: Glacial isostatic adjustment model with composite 3-D Earth rheology for Fennoscandia, *Geophysical Journal International*, 194, 61–77, <https://doi.org/10.1093/gji/ggt099>, 2013.
- van der Wal, W., Whitehouse, P. L., and Schrama, E. J.: Effect of GIA models with 3D composite mantle viscosity on GRACE mass balance estimates for Antarctica, *Earth and Planetary Science Letters*, 414, 134–143, <https://doi.org/10.1016/j.epsl.2015.01.001>, 2015.
- 615 Wang, H., Wu, P., and van der Wal, W.: Using postglacial sea level, crustal velocities and gravity-rate-of-change to constrain the influence of thermal effects on mantle lateral heterogeneities, *Journal of Geodynamics*, 46, 104–117, <https://doi.org/10.1016/j.jog.2008.03.003>, 2008.
- Wang, H., Jia, L., Steffen, H., Wu, P., Jiang, L., Hsu, H., Xiang, L., Wang, Z., and Hu, B.: Increased water storage in North America and Scandinavia from GRACE gravity data, *Nature Geoscience*, 6, 38–42, 2013.
- 620 Whitehouse, P., Latychev, K., Milne, G. A., Mitrovica, J. X., and Kendall, R.: Impact of 3-D Earth structure on Fennoscandian glacial isostatic adjustment: Implications for space-geodetic estimates of present-day crustal deformations, *Geophysical Research Letters*, 33, <https://doi.org/10.1029/2006gl026568>, 2006.
- Whitehouse, P. L.: Glacial isostatic adjustment modelling: historical perspectives, recent advances, and future directions, *Earth Surface Dynamics*, 6, 401–429, <https://doi.org/10.5194/esurf-6-401-2018>, 2018.
- 625 Williams, C., Lord, N., Lunt, D., Kennedy-Asser, A., Richards, D., Crucifix, M., Kontula, A., Thorne, M., Valdes, P., Foster, G., and McClymont, E.: The relative role of orbital, CO<sub>2</sub> and ice sheet forcing on Pleistocene climate, <https://doi.org/10.5194/egusphere-egu23-1048>, 2023.
- Wu, P.: Effects of lateral variations in lithospheric thickness and mantle viscosity on glacially induced surface motion in Laurentia, *Earth and Planetary Science Letters*, 235, 549–563, <https://doi.org/10.1016/j.epsl.2005.04.038>, 2005.
- 630 Wu, P. and Peltier, W. R.: Viscous gravitational relaxation, *Geophysical Journal International*, 70, 435–485, <https://doi.org/10.1111/j.1365-246x.1982.tb04976.x>, 1982.
- Wu, P., Wang, H., and Steffen, H.: The role of thermal effect on mantle seismic anomalies under Laurentia and Fennoscandia from observations of Glacial Isostatic Adjustment, *Geophysical Journal International*, 192, 7–17, <https://doi.org/10.1093/gji/ggs009>, 2013.

- 635 Yousefi, M., Milne, G. A., Love, R., and Tarasov, L.: Glacial isostatic adjustment along the Pacific coast of central North America, *Quaternary Science Reviews*, 193, 288–311, <https://doi.org/10.1016/j.quascirev.2018.06.017>, 2018.
- Yousefi, M., Milne, G. A., and Latychev, K.: Glacial isostatic adjustment of the Pacific Coast of North America: the influence of lateral Earth structure, *Geophysical Journal International*, 226, 91–113, <https://doi.org/10.1093/gji/ggab053>, 2021.